Progress in PHOTOVOLTAICS

PROGRESS IN PHOTOVOLTAICS: RESEARCH AND APPLICATIONS
Prog. Photovolt: Res. Appl. (2014)
Published online in Wiley Online Library (wileyonlinelibrary.com). DOI: 10.1002/pip.2556

29TH EU PVSEC, AMSTERDAM, THE NETHERLANDS, 2014

Design, fabrication and characterisation of a 24.4% efficient interdigitated back contact solar cell

Evan Franklin[1]*, Kean Fong[1], Keith McIntosh[2], Andreas Fell[1], Andrew Blakers[1], Teng Kho[1], Daniel Walter[1], Da Wang[1], Ngwe Zin[1], Matthew Stocks[1], Er-Chien Wang[1], Nicholas Grant[1], Yimao Wan[1], Yang Yang[3], Xueling Zhang[3], Zhiqiang Feng[3] and Pierre J. Verlinden[3]

[1] Australian National University, School of Engineering, North Road, Acton, ACT 0200, Australia
[2] PV Lighthouse, Coledale NSW, Australia
[3] State Key Laboratory of PV Science and Technology, Trina Solar, Changzhou, Jiangsu, China

ABSTRACT

The interdigitated back contact (IBC) solar cells developed at the Australian National University have resulted in an independently confirmed (Fraunhofer Institut für Solare Energiesysteme (ISE) CalLab) designated-area efficiency of 24.4 ± 0.7%, featuring short-circuit current density of 41.95 mA/cm^2, open-circuit voltage of 703 mV and 82.7% fill factor. The cell, 2 × 2 cm^2 in area, was fabricated on a 230 μm thick 1.5 Ω cm n-type Czochralski wafer, utilising plasma-enhanced chemical vapour deposition (CVD) SiN_x front-surface passivation without front-surface diffusion, rear-side thermal oxide/low-pressure CVD Si_3N_4 passivation stack and evaporated aluminium contacts with a finger-to-finger pitch of 500 μm. This paper describes the design and fabrication of lab-scale high-efficiency IBC cells. Characterisation of optical and electronic properties of the best produced cell is made, with subsequent incorporation into 3D device modelling used to accurately quantify all losses. Loss analysis demonstrates that bulk and emitter recombination, bulk resistive and optical losses are dominant and suggests a clear route to efficiency values in excess of 25%. Additionally, laser processing is explored as a means to simplify the manufacture of IBC cells, with a confirmed efficiency value of 23.5% recorded for cells fabricated using damage-free deep UV laser ablation for contact formation. Meanwhile all-laser-doped cells, where every doping and patterning step is performed by lasers, are demonstrated with a preliminary result of 19.1% conversion efficiency recorded. Copyright © 2014 John Wiley & Sons, Ltd.

KEYWORDS

high efficiency; silicon solar cell; interdigitated back contact; IBC; loss analysis

***Correspondence**

Evan Franklin, Australian National University, School of Engineering, North Road, Acton, ACT 0200, Australia.
E-mail: evan.franklin@anu.edu.au

Received 7 July 2014; Revised 3 September 2014; Accepted 9 September 2014

1. INTRODUCTION

Interdigitated back contact (IBC) cells [1–4], having both optical shading and front-side contacting requirements removed, are inherently capable of high efficiency. The first and most obvious advantage of IBC cells over front junction front contact cells is the complete removal of optical shading by metal fingers and bus bars, typically leading to around 5–8% higher current density. Secondly, the competing demands on the front emitter surface of front junction cells, which are required to simultaneously satisfy requirements of surface and emitter recombination, lateral conductivity and external contacting, can, to a large extent, be decoupled from one another in IBC cells by utilising an array of closely spaced, small local rear diffusion and/or contact features. This generally facilitates superior passivation of surfaces to be achieved while ensuring that rear diffusion and geometry can be designed to minimise recombination, lateral conductivity losses, current crowding and contact resistance. Furthermore, with rear contacted cells, the metal grid resistance can be almost eliminated as a significant resistive loss component because the full cell area is available for metal coverage, being also generally desirable from an optics perspective. IBC cells also present an opportunity to simplify module fabrication via novel technologies and materials such as the patterned conductive back sheet [5,6].

Copyright © 2014 John Wiley & Sons, Ltd.

Interdigitated back contact cells had long been widely regarded, along with silicon heterojunction (SHJ) technology [7,8], as the most likely cell type to surpass the previous 25.0% efficiency record [9] for silicon single-junction solar cells. Indeed, Panasonic recently reported a new world record of 25.6% (based on 125 × 125-mm substrate) based on a combination of the two technologies in the SHJ-IBC cell [10], with Sharp also reporting this year an efficiency of 25.1% (cell area approximately 4 cm^2) based on the same SHJ-IBC architecture [11] and SunPower reporting 25.0% (125 × 125 mm) for IBC cells using more standard surface passivation methods and manufactured on an industrial pilot line [12]. Recent progress has seen efficiency values reported for IBC cells fabricated in research institute labs of 23.0% at Fraunhofer ISE [13], 23.1% at Institut für Solarenergieforschung [14] and 23.3% at IMEC [15,16], all with 4-cm^2 cell areas. In the interests of advancing research-lab-based cells to a more industrially relevant processes Institut fur Photovoltaik has also reported a 22.0% efficient IBC cell with both emitter and back-surface field (BSF) doping performed by a laser process [17].

Following the early lead from SunPower [3], IBC cells are becoming increasingly considered as a promising route for large-scale industrial production, to continue the ongoing trend of increasing commercial efficiency. Hence, considerable attention is now being paid to the technology by a number of cell manufacturers [10–12,18–21]. Trina Solar, a collaboration partner on IBC cell development with the Australian National University (ANU), recently reported large-area cells with independently confirmed 22.1% efficiency on 125 × 125-mm Czochralski (Cz) substrates and in-house measured 23.2% efficiency on 156 × 156-mm Cz substrates [18,19], and both Bosch and Samsung have reported on the development of large-area IBC cells utilising ion implantation to achieve 22.1 and 22.4% respectively [20,21].

The development of IBC cells at ANU is targeted firstly at realising the highest lab-scale cell efficiency practically possible and secondly at using the knowledge gained to subsequently incorporate fabrication simplifications and industrially applicable processes to achieve high-efficiency industrial IBC cells. This paper describes an approach to cell development based on systematic process improvement and cell design optimisation. An iterative approach is used whereby as the optimisation of key fabrication processes are progressed, for example, the critical rear-surface passivation stack, simultaneously, the cell design is optimised. This relies upon rigorous collection of all relevant process data (for example, the recombination parameters, surface doping characteristics and contact resistivities of each of the various rear-side features), followed by optical and device modelling to tailor cell design to the known process outcomes.

2. CELL DESIGN AND KEY FEATURES

A two-dimensional representation of an IBC cell, typical of those fabricated in ANU's laboratories, is shown in Figure 1. This is, in fact, one particular variant of IBC cell design, where there is no front diffusion (no front-surface field (FSF)), where *n*+ base contacts and BSF diffusion are both localised, but where p+ emitter coverage is relatively large with a small fraction of p+ contact points. Alternative IBC cell designs have long been proposed by various authors [1,22]. Figure 2 shows four variants on rear-surface design investigated at ANU. In each of the cases shown, the n+ and p+ metal contact layout remains identical, while the associated doped regions vary in shape. This clearly represents another design variable. While there is a general desire to have a large emitter coverage and a small undiffused region or gap between emitter and BSF, at least for ensuring high minority carrier collection efficiency [23], as shown in the lower design, this requires dielectric films with absolutely no imperfections such as pinholes or micro-cracks that could lead to direct shunting. Such a film requires typically the deposition of a thick, possibly multi-layer, dielectric, as reported for example in Aleman *et al.* [16] or in the case of this work a thin double-layer dielectric stack with superb isolation properties. One difficulty can be that such a film may be impractical or difficult to fabricate reliably, while still achieving the desired optimum passivation properties. The rear-surface design consisting of localised doping and localised contacts for both emitter and BSF is of particular interest for future industrial IBC cell research at ANU and forms

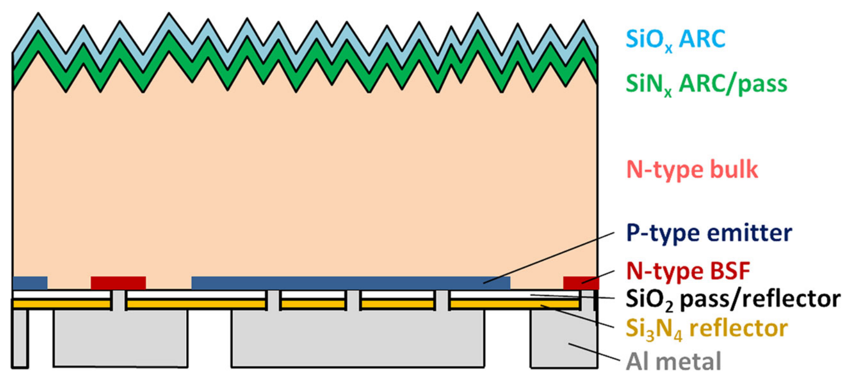

Figure 1. Two-dimensional, cross-section representation of the IBC cells fabricated in this work.

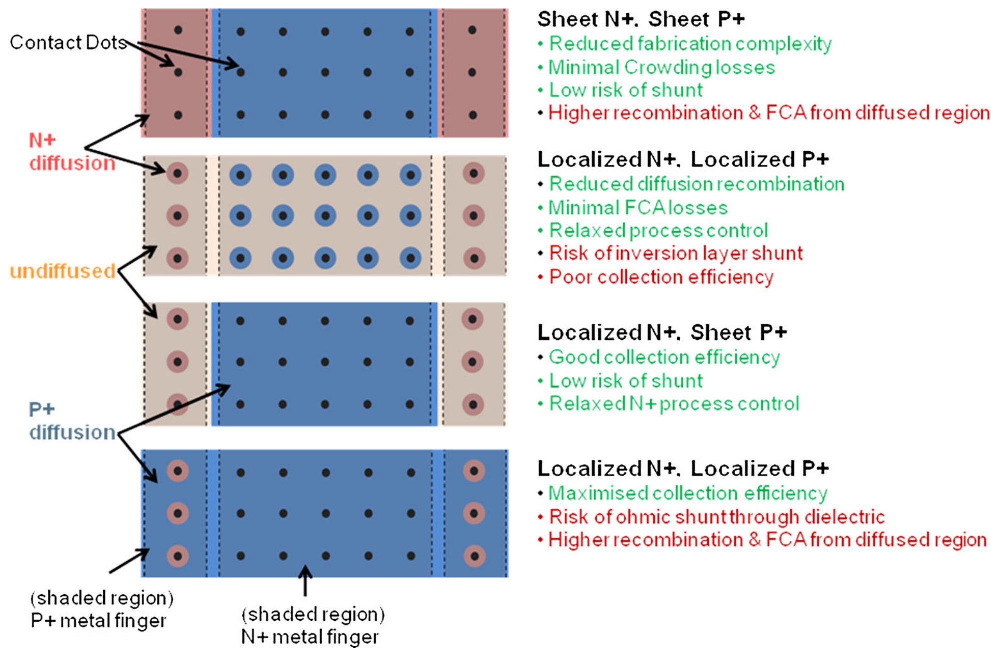

Figure 2. Primary variants on design of rear-surface diffusion, with fixed local contact opening pattern: Sheet n+/sheet p+ (top), local n +/local p+ (mid-top), local n+/sheet p+ (mid-bottom), sheet n+/full-area p+ (bottom).

the basis for the all-laser-doped IBC cells reported in this paper. Localised laser processes can lead to higher throughput in manufacturing (smaller laser processed area and lower laser energy required per wafer) and are more compatible with optimal cell design where recombination at laser-doped regions is typically larger than furnace diffused and passivated regions [24]. This is in contrast to the laser-doped cells of Dahlinger *et al*. [17] that instead utilise large-area laser-doped emitters with subsequent photolithographically defined small localised contact openings.

The general design objectives for the IBC cell or indeed any solar cell are relatively straightforward: to maximise the amount of light coupled into and absorbed within the active cell area, to maximise carrier collection at the p–n junction (and, conversely, to minimise recombination in the bulk and at all surfaces), and to minimise resistive losses both within and external to the active cell area. Maximising carrier generation requires excellent front-surface texture and anti-reflection coating and suggests thicker cells for maximum path length at long wavelengths. For IBC cells, where carrier collection occurs at the rear surface, this necessitates use of material with high minority carrier lifetimes and outstanding front-surface passivation. A detailed study of the trade-off between material quality, wafer thickness, resistivity and front-surface passivation is required to realise the optimum material for IBC fabrication. Such an approach has been detailed by various authors previously for IBC cells [25,26]. While these aspects of design are discussed in this paper, it should be noted that cells fabricated as part of this work are based on the best material quality and front-passivation scheme available at the time at ANU; the focus for design optimisation therefore shifts primarily to rear cell design.

The rear silicon surface of IBC cells considered here consists essentially of five distinct interfaces (bulk undiffused region and passivation film, n+ doped region and passivation film, n+ doped region and metal, p+ doped region and passivation film, and p+ doped region and metal). Optimisation of the rear surface as a whole requires co-optimisation of these five regions. This necessitates a detailed study to determine the doping level and coverage fraction of each diffusion type, along with the contact opening fraction that will yield low contact and current-crowding resistance, low recombination current and high collection efficiency for optimum cell performance, using data known for the best available combinations of passivation films and processes.

2.1. Optical design

Optical considerations for IBC cells do not differ greatly from those for any other cells: the objective always being to maximise transmission at the front outer surface of the cell and to maximise optical path length within the cell. However, properties of IBC cells mean that these can be more readily achieved: no front metallisation translates to less shading but also means that anti-reflection schemes can be designed and implemented independently of contacting considerations; rear-surface passivation dielectrics and near to full area metallisation can ensure highest possible rear reflection, while for the case of localised small area fraction, rear-contact front and/or rear-surface

texturing can be achieved relatively unencumbered by the requirements of contact formation.

We employ OPAL 2 [27] to assess the front-surface optics and the Wafer Ray Tracer to assess the internal optics [28,29]. These programmes incorporate ray tracing and the transfer matrix method to rapidly quantify the optical losses of the IBC cell. Results relevant to the optimisation of the IBC cell are shown in Figures 3–5.

Figure 3 plots the front-surface optical losses in terms of an equivalent photon current under a normally incident unpolarised AM1.5G spectrum. The losses are calculated for random pyramids with a base angle of 53° and variable thicknesses of plasma-enhanced chemical vapour deposition (PECVD) SiN_x and PECVD SiO_x. The refractive index of these materials was presented in McIntosh *et al.* [29]. Figure 3 shows that a photogeneration current gain of 0.4 mA/cm^2 can be achieved by utilising a double-layer anti-reflection coating (ARC) consisting of a 65-nm layer of SiN_x below a 90 nm of SiO_x, as compared with a single-layer PECVD SiN_x ARC.

Figure 4 plots the internal reflection as a function of wavelength for unpolarised light impinging on a planar rear surface at 40°. This is the incident angle for the first-pass light that reaches the rear under the conditions described for Figure 3. The simulations were performed for 30 nm of SiO_2 layer under a variable thickness of low-pressure CVD (LPCVD) Si_3N_4, beneath 3 μm of pure Al. The figure shows that for the experimental cell, which had 30 nm SiO2 and 90 nm of Si_3N_4, the first-pass internal reflection is 95–96%. This could be increased above 99% by thickening the Si_3N_4 to >200 nm. The previously mentioned results are relevant to most IBC cells reported in the literature, which feature a random pyramid textured front surface and a planar or quasi-planar rear. One possible exception is SunPower's so-called Generation 3

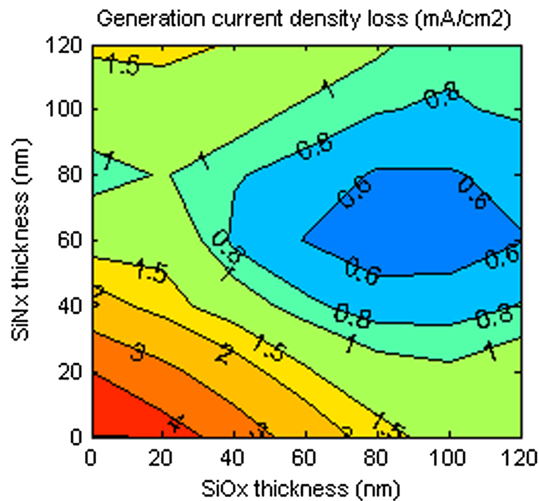

Figure 3. Modelled optical loss, expressed as a potential photogeneration current density (mA/cm^2), as a function of front-surface SiO_x on SiN_x double-layer anti-reflection coating film thicknesses on a random pyramid textured surface.

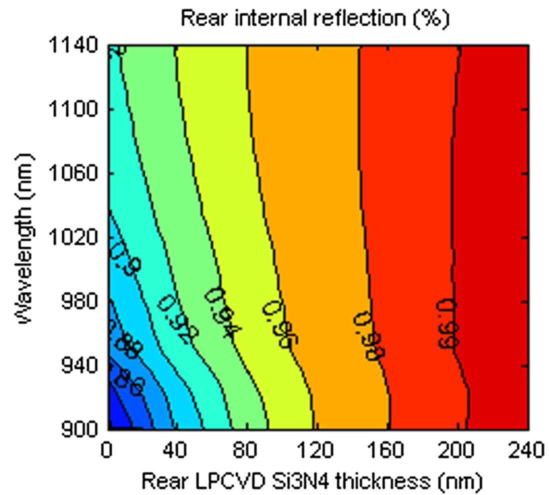

Figure 4. Modelled internal reflection at rear planar surface consisting $Si/SiO_2/Si_3N_4/Al$ stack as a function of Si_3N_4 thickness with fixed SiO_2 and Al thicknesses of 30 nm and 3 μm respectively and assuming normal incident light on a random pyramid front-surface texture.

cell, where it is suggested but not explicitly stated that the rear surface is textured between contact regions [3].

In Figure 5, we show the gain in photogeneration current that could be achieved for a range of front and rear-surface textures, treatments and dielectric films on a 230-μm-thick cell. Surface textures are referred to in the figure as 'rantex' for random pyramid texture, 'invtex' for inverted pyramid texture, 'x grooves' for V-shaped grooves in 'x' direction, and 'y grooves' for V-shaped grooves in direction perpendicular to the 'x' direction. Changing from a purely planar rear surface to random pyramid textured rear yields a gain as much as 1.1 mA/cm^2. Cells produced at the ANU to date are based on a planar rear surface, although a fabrication sequence giving a textured rear has been proposed in Zin *et al*. [30].

2.2. Wafer quality, resistivity and thickness

Substrate quality, best quantified via bulk minority carrier lifetime at the end of processing, is widely regarded, along with front-surface passivation quality, as one of the two key parameters that can limit performance of rear junction cells. McIntosh *et al.* first highlighted the critical dependence of efficiency on high-lifetime material [31], with subsequent modelling by Cousins *et al*. suggesting that bulk lifetime greater than 10 ms and front-surface recombination current prefactor, J_0, less than 10 fA/cm^2 are required to achieve 25+% IBC cells [3]. While fabrication of cells in this work was limited to a small selection only of available wafer types, we extend the modelling approach by applying 3D device simulations to show the impact of bulk resistivity, bulk lifetime and wafer thickness on achievable IBC cell efficiency. Simulations are thus conducted in the first instance with variable wafer resistivity and thickness, and Auger-limited bulk recombination only,

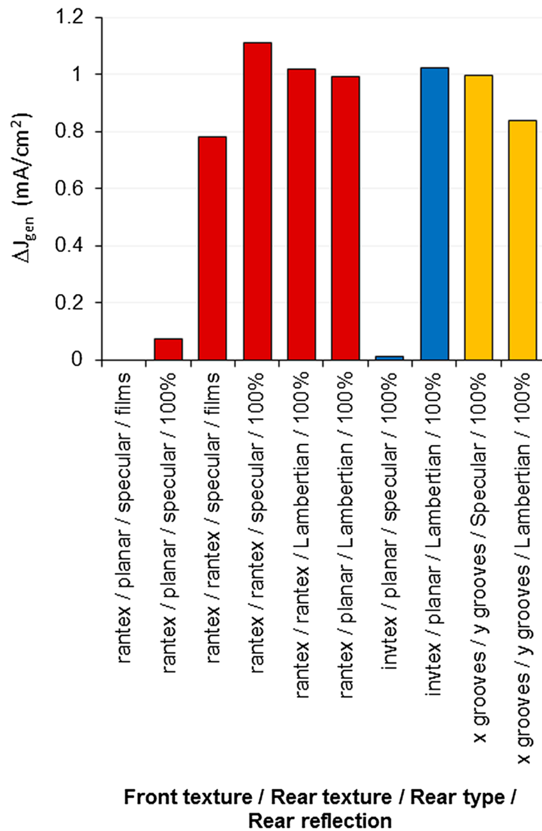

Figure 5. Gain in photogeneration current density (mA/cm^2), from optical modelling, for a range of possible IBC cell front and rear-surface treatments ('rantex'—random pyramid texture, 'invtex'—inverted pyramid texture, 'x grooves'—V-shaped grooves in 'x' direction, and 'y grooves'—V-shaped grooves in direction perpendicular to 'x' direction) in comparison with a 'base case' consisting of random pyramid textured front surface and planar rear surface with specular reflection from a 30/90-nm SiO_2/Si_3N_4 stack, as used for cell fabrication in this work. Normally incident AM1.5G spectrum, a near-optimum front-surface double-layer ARC and a 230-μm-thick cell are assumed for ray tracing.

and in the second instance with variable electron and hole Shockley–Read–Hall (SRH) lifetime, τ_{n0} and τ_{p0}, and wafer thickness. Surface recombination parameters equivalent to the best achieved cell in ANU labs to date are applied to passivated surfaces—5 fA/cm^2 for the front surface, 15 fA/cm^2 for the undiffused rear surfaces, 20 fA/cm^2 for the 200 Ω/□ rear emitter surfaces, and 120 fA/cm^2 for the 30 Ω/□ local rear BSF surfaces—with contacts arranged such that both contact recombination and contact resistivity have negligible influence. An 'external grid' series resistance of 0.2 Ω cm^2 is used; no significant shunts are included. While wafers fabricated in this work are performed on 180–230 μm thick, 1.5 and 2.5-Ω cm material, Figure 6 suggests that an efficiency gain of 0.3% absolute or higher could be expected if thicker, high-resistivity wafers are used, provided that high carrier lifetimes can be achieved.

2.3. Front-surface passivation

Because the highest rate of carrier generation occurs near to the front surface and because carrier collection at the p–n junction of IBC cells occurs at the rear, the front surface plays a crucial role in ensuring both high collection efficiency and minimal carrier transport resistive loss. The majority of IBC cells reported in literature to date [13,15,17,32] feature a passivated FSF to ensure excellent front-surface passivation. However, more recently, IBC cells without FSF are being reported by various research groups [14,25]. In cells produced in this work, pitch is smaller than 500 μm, BSF coverage fraction is small, and bulk resistive losses are reduced via conductivity modulation [33], meaning that any lateral transport benefits that might otherwise result from inclusion of a moderate to heavily doped FSF [34] will be negligible. The question then is purely what combination of front-surface doping and passivation film provides the minimum level of front-surface recombination while still meeting the objectives of the optical design. At ANU, improved understanding of deposition parameters has led to outstanding surface passivation of undiffused silicon via PECVD SiN_x, with minority carrier lifetimes at the intrinsic limit demonstrated on SiN_x-passivated 0.47-Ω cm n-type material [35]. The same film has also been demonstrated to have ultralow absorption. For purposes of modelling and optimising IBC cells in this work, we quantify the surface passivation quality in terms of recombination current prefactor, J_0, extracted from quasi-steady-state photoconductance measurements according to the method of Thomson *et al.* [36] that builds on the well-known method of Kane and Swanson [37] by resolving the local carrier density across the sample thickness rather than assuming a uniform profile. Figure 7 plots the measured minority carrier lifetime curve for the symmetrically textured, undiffused and passivated 1.5-Ω cm n-type wafers used in the fabrication of IBC cells in this work, along with the modelled fit yielding a J_0 value of 5 fA/cm^2, assuming an effective intrinsic carrier density $n_{i,eff}$ of 8.70×10^9 cm^{-3}, determined according to Schenk's model of band gap narrowing [38] and temperature corrected as described in Richter *et al.* [39] for 1.5-Ω cm n-type material at 25°C. This value for $n_{i,eff}$ is consistently used throughout this work.

2.4. Rear-surface diffusion and passivation

The rear surface of IBC cells consists generally of five distinct surface regions: undiffused, phosphorus diffused and passivated, phosphorus diffused and metallised, boron diffused and passivated, and boron diffused and metallised. Rear-surface recombination can thus only be minimised by considering each of these regions and ensuring that the net effect is optimised, bearing in mind that recombination owing to each diffused region consists of surface recombination and recombination in the diffused layer itself. Recombination owing to the metallised, diffused regions is essentially a function of total surface dose [40] or, for

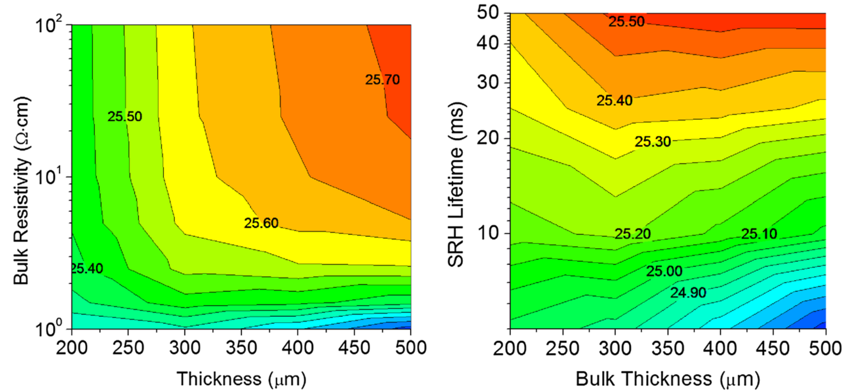

Figure 6. Influence of bulk resistivity and wafer thickness (left) and bulk SRH lifetime and wafer thickness (right) on achievable IBC cell efficiency, modelled using Quokka 3D device simulator [42]. Device simulations are based on the IBC cell structure indicated by Figure 1, used best results achieved to date in ANU labs for relevant passivation characteristics of each surface region and used photogeneration profiles determined for each thickness by optical ray tracing. Investigation of the influence of wafer resistivity and thickness (left) assumes bulk recombination to be limited only by Auger and radiative recombination, while the investigation of the dependence upon bulk SRH lifetime (right) is based on a bulk resistivity of 2.5 Ω cm.

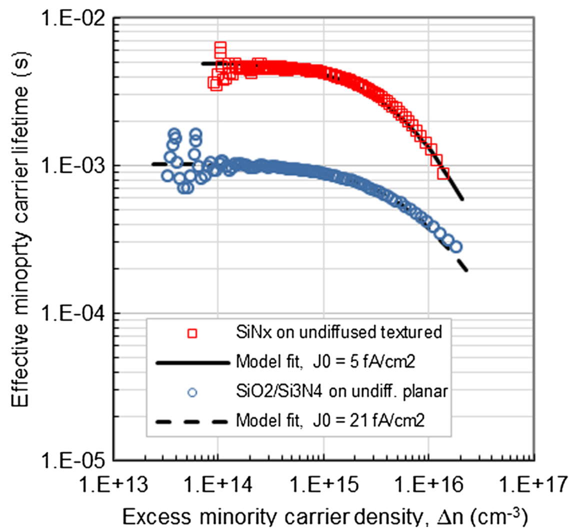

Figure 7. Minority carrier lifetime as a function of carrier injection, via QSSPC measurement, for PECVD SiN_x passivated textured and SiO_2/LPCVD Si_3N_4 passivated planar surfaces on undiffused 2.5 and 1.5-Ω cm n-type wafers respectively. The surfaces, which represent the front surface and undiffused rear-surface regions respectively of IBC cells fabricated as part of this work, can in each case be parameterised by an injection-independent recombination current prefactor, J_0, of 5 and 21 fA/cm^2.

the case of comparing diffusion of similar depth, sheet resistance. Recombination at passivated diffused regions meanwhile depends upon both the doping level and the passivation film, and likewise, for undiffused regions, the recombination is chiefly governed by the surface passivation film. One approach for optimising rear-surface passivation is to use multiple surface passivation films, each tailored to the properties of the underlying surface but at the expense of considerable fabrication complexity. Our approach is to use a film stack that is capable of simultaneously providing excellent passivation on all three surface types.

In this work, we use a stack consisting of a thin thermally grown silicon dioxide (SiO_2) beneath a LPCVD of stoichiometric silicon nitride (Si_3N_4), which was chosen because it preserves or improves the surface passivation that can be achieved with thermally grown silicon dioxide and is well known for having excellent chemical etch resistance [41] and also because it exhibits outstanding electrical isolation properties. This latter property becomes particularly important for IBC cells where the base and emitter doping regions do not correspond to the n and p metallisation regions, which may be either desirable for improving net passivation and/or for minimising the electrical series resistance owing to the external metal finger pattern. Such a requirement has led some research groups to the use of a thick (in the order of 1500 μm) PECVD SiO_2 film as an isolation layer [13] or to incorporation of spin-on organic layers such as polyimides to provide the necessary isolation [30]. We use film stacks consisting of a thin thermal oxide (~30 nm) grown at 950°C in O_2 ambient, followed by 45-min 1000°C N_2 anneal for superior passivation underneath an LPCVD silicon nitride deposited at 775°C to a thickness typically of 80–100 nm, to provide very good surface passivation while also yielding excellent electrical isolation.

The same oxide/nitride film stack when used for purposes of passivation of boron and phosphorus diffusion yields the results shown in Figure 8. Here, several phosphorus and boron diffusion has been prepared on symmetrically diffused and passivated high-resistivity wafers, with recombination current prefactor J_0 subsequently extracted using the method after Thomson *et al.* [36]. Also included on the plots are the J_0 values measured for the same diffusion subsequent to metallisation, achieved in this case by removing the dielectric stack and evaporating a layer of

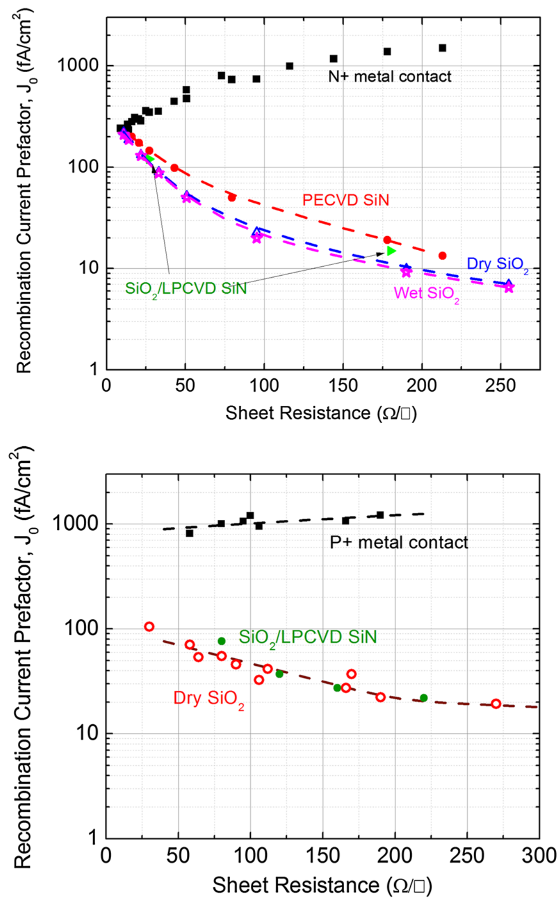

Figure 8. Measured recombination current prefactor, J_0, as a function of phosphorus doping (top) and boron doping (bottom), for both thermal SiO_2/Si_3N_4 passivated and for metallised surfaces. Recombination characteristics are also shown for passivation by thermal oxide and in the case of phosphorus diffusion by steam oxide and PECVD SiN_x.

no more than a few nm of aluminium. Such a method allows the same pitch circle diameter measurement to be used, with the vast majority of incident light passing through the thin aluminium layer and with the reflection coefficient adjusted accordingly. These plots show that the passivation quality of the oxide-only film is preserved after nitride deposition, with this set of data now giving guidance for optimisation of the IBC cell rear. Finally, we are also able to quantify the surface passivation characteristics for the same oxide/nitride stack on planar undiffused 1.5-Ω cm n-type wafers used in this work, with lifetime data provided in Figure 7. Recombination is well characterised by an injection-independent recombination current prefactor J_0 of 21 fA/cm^2, using $n_{i,eff} = 8.70 \times 10^9$ cm^{-3}, the injection independence most likely owing to field effect induced by trapped charge in the film. In a later publication, it will be shown that surface recombination is influenced heavily by the LPCVD deposition parameters and the oxide and nitride thickness, although in this work, a single deposition recipe is exclusively used.

2.5. Contact resistivity

The remaining information required for full IBC cell rear-surface design optimisation is the contact resistivity data for the same boron and phosphorus diffusion. We metallise by evaporation of aluminium at high vacuum, achieving excellent contact by ensuring that a high evaporation rate is achieved prior to target wafers being exposed to the evaporant, and via a subsequent 30 min sinter at 250°C in a forming gas ambient. Contact resistivity is measured via isolated linear transfer length method structures [42]. The resultant contact resistivity measurements for a range of sheet resistances for both phosphorus and boron diffusion are plotted in Figure 9, with the lines of best fit subsequently used in rear optimisation. To put these values into context with the IBC cells fabricated as part of this work, a specific contact resistivity of 2×10^{-5} Ω cm^2 for each contact type equates to a total cell level contact resistance of 0.024 Ω cm^2, assuming n and p contact fractions of 0.11 and 0.33% respectively. This, in turn, corresponds to a loss in cell efficiency of 0.04% absolute.

2.6. 3D modelling approach to design optimisation

We approach detailed IBC cell design in this work via cell performance optimisation based on the 3D device modelling using Quokka [43], which uses the conductive boundary approach [44] to define each surface in terms of the measurable quantities described in this paper. We have shown previously that there is little difference in optimum cell performance, between localised BSF and a broader area BSF confined to the region beneath the n + finger, provided that surface recombination behaviour is similar for lightly diffused and undiffused regions and pitch is small enough to ensure high emitter collection efficiency [4]. However, in the case of localised BSF diffusion, the

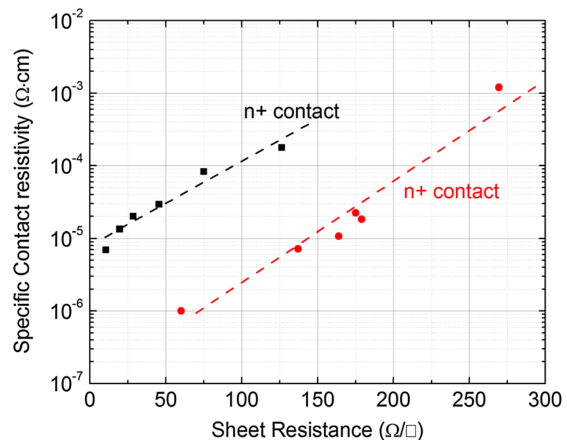

Figure 9. Contact resistivity, measured via transfer length method structures, of evaporated aluminium contacts on phosphorus and boron diffusion.

doping levels corresponding to the optimal design cover a wider range; additionally, the localised BSF scheme facilitates the incorporation of anticipated improvements in passivation of undiffused surfaces. In the optimisation conducted for cells fabricated in this work, cell pitch, contact size and contact pitch are generally fixed. Future optimisation could include rear contacting layout as a variable, facilitated, for example, by fully flexible damage-free laser ablation (outlined later in this paper), but in this work, we are limited by the availability of photolithography masks. Further device modelling is thus undertaken under the assumption of fixed localised contact layout for both n and p contacts (~7.5-μm-diameter contact openings on a 70-μm pitch) and wafer thickness of 200 μm.

Determination of the optimal boron diffusion fractional area and doping level is illustrated by the plot of modelled cell efficiency in Figure 10, with a band of optimal parameters between around 180 and 220 Ω/□ at emitter fractions above about 60%. For heavier diffusion, surface recombination at the passivated surfaces starts to dominate, overcoming any gains made from reduced recombination at contacts and from reduced contact resistance. In contrast, the increase in both resistive loss and recombination at contacts dominates over the marginal reductions in recombination at passivated surfaces as diffusion samples are made lighter. For decreasing emitter fractions, the sensitivity to emitter diffusion is reduced, albeit for a reducing peak efficiency, until at less than about 5% coverage, current crowding losses start to become significant as emitters become local diffusion surrounding each contact. The simulations lead to a rear design as shown in Table I, for

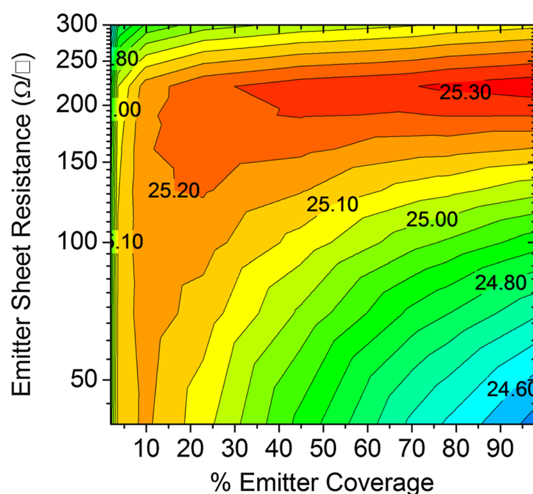

Figure 10. Modelled cell efficiency as a function of emitter diffusion sheet resistance and diffusion fraction, based on recombination characteristics presented for passivation of diffused and undiffused areas and measured contact resistivities. Modelling is based on 200-μm-thick, 2.5-Ω cm n-type wafers with local phosphorus BSF; a bulk SRH lifetime of 10 ms is assumed, and no edge losses are considered.

cells fabricated with 500-μm finger pitch on 200-μm-thick 1.5-Ω cm n-type material. This design would require re-optimisation for any significant process improvements.

3. CELL FABRICATION PROCESS

Fabrication of IBC cells at ANU, for the cell design as described previously, requires several masking and patterning steps. To achieve high cell efficiency, this requires damage-free patterning, and hence, photolithography is used extensively in cell fabrication. Figure 11 summarises the fabrication sequence employed at ANU to create IBC cells with localised phosphorus diffused n +contacts and large emitter coverage, which is also described in some detail in the succeeding texts. In fabrication of cells so far, n-type materials with resistivity at least greater than 1 Ω cm and with high minority carrier lifetimes are chosen. Importantly, material is selected on the basis of minority carrier lifetime after the typical sequence of high-temperature diffusion and oxidation steps employed in the fabrication process. Effective minority carrier lifetimes in excess of 3 ms are observed, via HF passivation technique [45], for both 2.5 Ω cm float-zone (FZ) and 1.5-Ω cm Cz wafers after exposure to such a sequence.

Fabrication commences with a saw-damage etch using an 85 °C 50% *v*/*v* tetramethylammonium hydroxide (TMAH) solution, to remove approximately 10–15 μm from each wafer surface (step 1 in Figure 6), followed by standard RCA clean (RCA1 and RCA2). A thin masking SiO_2 (approximately 15 nm, grown at 950°C) and LPCVD Si_3N_4 (40 nm) stack is then formed (step 2) prior to photolithography, plasma etch and BHF etch to define a pattern of ~27-μm-diameter openings aligned along each of what will eventually become the regions beneath the n + metal fingers that are at a pitch of 500 μm (step 3). After standard RCA clean, phosphorus doping in these openings is achieved via a conventional tube furnace $POCl_3$ diffusion recipe to yield the required doping level (in our ‘optimum’ case approximately 30 Ω/□ following all subsequent thermal treatments, yielding a surface concentration in the order of 4×10^{19} cm^{-3} and depth greater than 1.5 μm). Note also that the full-area front surface is simultaneously diffused during this step, providing an effective degree of contaminant gettering [46] (step 4). The phosphosilicate glass and remaining dielectrics are removed in dilute HF solution (step 5) prior to growth of a thick SiO_2 masking layer (step 6)—a 25-min 1000°C steam oxidation, yielding approximately 200 nm on undiffused surfaces and somewhat thicker on phosphorus-diffused surfaces.

Photolithography and BHF etch (step 7) are required to create windows for subsequent standard RCA clean and boron emitter doping via conventional BBr_3 tube diffusion (step 8) to yield a sheet resistance of approximately 200 Ω/□ following all thermal processing (surface concentration of around 1×10^{19} cm^{-3} and junction depth greater than 1 μm). It is at these two steps that emitter coverage is easily adjusted by choice of photomask, from ~1% coverage (localised diffusions

Table I. Requirements for optimum rear cell design, via 3D modelling optimisation based on metrics for best available process at time of optimisation.

Rear-surface region	Coverage %	Required sheet resistance (Ω/□)	Expected J_{0e} (fA/cm^2)	Expected contact resistivity (Ω cm^2)
Passivated n + region	2	30	150	—
Metallised n+ region	<0.2	30	300	2×10^{-5}
Passivated p+ region	>50	200	25	—
Metallised p+ region	<0.75	200	1000	7×10^{-5}
Undiffused region	~30–50	—	20	—

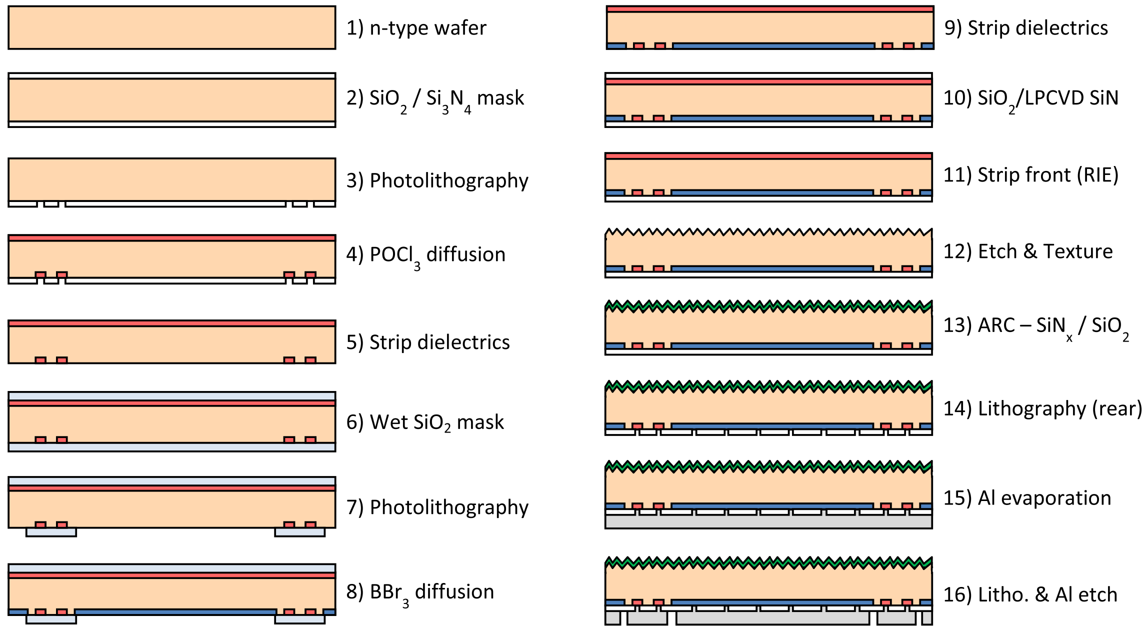

Figure 11. Summary of fabrication sequence at ANU for IBC cells with localised n+ BSF and contacts and sheet emitter with local contacts.

at contacts) up to ~100% coverage (emitter diffusion surrounding local BSF), with emitter diffusion being correspondingly altered to suit. The borosilicate glass and masking dielectric are next removed in dilute HF (step 9) prior to RCA cleaning, growth of thin passivation oxide and deposition of LPCVD Si_3N_4 capping layer (step 10). This dielectric stack is preferred for the rear surface because the thermal oxide provides excellent passivation on all three surface types (phosphorus diffused, boron diffused and undiffused), which is maintained or improved upon by subsequent silicon nitride deposition, and because the outstanding chemical etch resistance and electrical isolation properties of the LPCVD Si_3N_4 mask provide flexibility for subsequent wafer processing and metallisation. Oxidation is conducted at 1000°C in dry O_2 with subsequent N_2 anneal to yield 30-nm oxide thickness on undiffused or boron-diffused surfaces, and nitride deposition takes place at 775°C using a 1:4 ratio of dichlorosilane : NH_3 to produce an approximately 100-nm-thick film. The passivation qualities of this film stack across the range of surfaces are one of the key reasons for the high efficiency results at ANU; preliminary indications from experiments with varied growth and deposition conditions suggest that there is considerable room for further improvement and hence refinement of cell rear design.

The passivation/masking stack is stripped from the front surface via an unmasked plasma etch (step 11), with the phosphorus-diffused layer then removed in an 85°C TMAH etchant solution prior to random pyramid formation via a TMAH/isopropyl alcohol texturing solution (step 12). Front-surface passivation and anti-reflection coating film or films are then deposited via PECVD (step 13). The SiN_x process developed and optimised at ANU [35] provides outstanding surface passivation, while an optional PECVD SiO_x can then be deposited on top to provide improved anti-reflection properties via the so called double-layer ARC (DLARC). In fact, for the best cell reported in this paper, a 75-nm SiN_x film was deposited at this step with the subsequent 80-nm SiO_x deposition occurring after the completion of cell metallisation. Photolithography is again used to open

7-μm-diameter contact windows, corresponding either to the centre of the localised phosphorus diffusion or otherwise spaced approximately 70 μm apart throughout the boron-diffused p finger regions (step 14). Low-resistivity contacts are achieved via rapid aluminium evaporation, with multiple evaporation sources, to deposit approximately 3–3.5 μm of aluminium across the entire rear surface (step 15). Metallisation is completed by a contact separation etch to isolate the emitter and base contacts, using a phosphoric-acid-based Al etchant solution, after fingers and bus bars are defined via a final photolithography step (step 16). Cells are tested both before and after a 250°C forming gas anneal, which generally improves contact adhesion, lowers contact resistivity and ensures good front-surface passivation.

All lithography masking is such that diffusion and n and p fingers are each defined within a $2 \times 2\text{-cm}^2$ active cell area, while the relatively wide bus bars, required to ensure good alignment to test jig probes, are 'floating' on top of the rear dielectric and are outside the cell active area. Illuminated IV testing is thus carried out using a precision-aligned aperture mask that is non-transparent across the whole spectrum.

3.1. Process simplification via laser processing

The process described previously is designed with maximum cell efficiency in mind and with little regard for industrial feasibility. Indeed, the complexity of the process, in particular the multiple photolithographic patterning steps, renders it prohibitively expensive for large-scale commercial manufacturing. Industrially relevant manufacturing process for IBC cells is thus being pursued variously by research groups and companies alike [15,18,20,47,48]. At ANU, we are investigating the use of laser processing as a means of reducing fabrication complexity and creating an industrially relevant process. This work falls into two categories: damage-free laser ablation for wafer patterning and laser doping for replacement of patterning and diffusion.

Laser ablation has been most commonly used in IBC cell research to date for direct patterning of wafers prior to diffusion, such as in the so-called RISE cell [48]. In this context, the requirements of the laser process are typically not high because typically, it is followed by a damage etch prior to diffusion. At ANU, we focus first on the most challenging application of laser ablation—the direct replacement of photolithography for contact formation on existing diffusion. The requirements of the laser process are that the overlying dielectric be removed to enable low-resistivity contact formation without introduction of any significant electronic damage to the underlying silicon. The expensive multi-step lithography process can then be replaced by a single laser process. Such an approach has been reported by Engelhart *et al.* [49] using a 532-nm picosecond laser for direct ablation of SiO_2 and similarly by O'Sullivan *et al.* [15] using a 355-nm picosecond laser for IBC cell contact formation, showing that photolithography can be replaced by direct picosecond laser ablation with a relatively modest reduction-only recombination or in V_{OC} and efficiency respectively. Engelhart *et al.* also reported in the same study that use of a 532-nm nanosecond laser for indirect ablation introduced significant damage, evidenced by measurements of vastly increased recombination current prefactors after laser processing compared with a chemically etched reference sample. Knorz *et al.* [50] meanwhile have demonstrated damage-free ablation of SiN_x from textured surfaces using 355-nm nanosecond laser. In this work, we achieve damage-free ablation using an excimer 248-nm nanosecond laser, capable of delivering multiple homogenous small area pulses via a projection mask inserted into the beam path. Extensive details on the damage-free excimer ablation process and analysis are provided by Walter in Walter *et al.* [51], which demonstrates that not only is the 248-nm nanosecond laser well suited to selective removal of silicon nitride but also surface recombination is essentially unaltered by the ablation process and that contact resistivity is at the level expected for the underlying diffusion over a range of laser fluences. Recombination current prefactors, J_0, of 750 and 1160 fA/cm^2 respectively were measured for locally opened features on phosphorus and boron-diffused surfaces following excimer laser ablation of a passivating oxide/nitride dielectric stack at the fluence of 1.7 J/cm^2 used subsequently for cell fabrication in this work. These values can be compared directly with measured values of 700 and 1300 fA/cm^2 for similar phosphorus and boron-diffused surfaces after passivating films have been removed by chemical etch. In the fabrication process described by Figure 11, steps 3, 7 and 14 could all be replaced by this direct laser ablation process. However, in cells fabricated as part of this work, we report on replacement of step 14 only with a single pulse laser ablation process, using a contact opening with approximately 50% larger diameter than that produced via photolithography.

Replacement of both boron and phosphorus diffusion on the rear surface of IBC cells with laser-doped features, combined with no requirement for a diffused FSF, offers the opportunity not only for greatly reduced manufacturing complexity but also for the elimination entirely of high-temperature processing steps. Taking a similar approach to that presented by Dahlinger *et al.* [17], in this work, we first separately apply boron and phosphorus dopant precursors, in this case, proprietary spin-on dopant films from Filmtronics Inc. [52] and laser irradiate to introduce dopants into the rear surface, prior to depositing a rear dielectric passivation layer and subsequently creating contact openings within the laser-doped regions. In contrast to Dahlinger *et al.*, we create a pattern of small, localised emitter and BSF regions, and we also utilise laser ablation rather than photolithography for aligned contact formation. Doping and ablation are both achieved using the same 248-nm nanosecond laser system, primarily driven by the requirement to ensure perfect alignment between the doped region and contact openings, having sizes of $30 \times 30\,\mu m^2$ and $18 \times 18\,\mu m^2$ respectively. Doping in this work was conducted in all cases with a fluence of 1.8 J/cm^2, selected on the basis of preliminary assessment

of recombination properties of boron-doped test structures. However, this yielded only very lightly doped boron and phosphorus regions, sheet resistances of about 250 and >1000 Ω/□ respectively being observed on test structures, with very poor contacts being subsequently observed for most fabricated cells. With reference again to Figure 11, the complete fabrication process can be described by replacing steps 1 to 9 with these phosphorus and boron laser doping processes, the remaining processing steps being identical with the exception of step 14 that is also replaced by aligned, direct excimer laser ablation for contact formation.

4. IBC CELL RESULTS

4.1. Photolithography based 24.4% efficient cell

Based upon a rear cell architecture consisting of localised n+diffusion and sheet p+emitter diffusion, produced according to the design and fabrication sequence described herein (albeit with final sheet resistances of 19 and 166 Ω/□ respectively, below the previously quoted target values), small batches of IBC cells have been successfully fabricated at ANU on both Cz and FZ n-type material. The best produced cell had independently confirmed designated-area (4 cm^2) efficiency 24.4% + −0.7%, measured at Fraunhofer CalLab, fabricated on a 1.5-Ω cm Cz wafer with final thickness of 230 μm. This cell had 330-μm-wide boron emitters (an emitter coverage fraction of 66%), localised BSF with diameter of 27 μm on a 70-μm pitch (for a total BSF coverage fraction of 1.9%), and 7-μm-diameter contact openings on a 70-μm pitch to yield n and p contact fractions of 0.13 and 0.43% respectively. Figure 12 shows the IV curve data for this cell, along with measured reflectivity, external quantum efficiency and internal quantum efficiency (IQE) curves. The cell exhibits very little front reflection and has outstanding collection efficiency, calculated from reflectivity and quantum efficiency to be 98.2% (averaged over the 600 to 900-nm range).

Four 2×2-cm cells were fabricated for each wafer, each having slightly different rear-surface geometry. Of these, some were consistently shunted, owing to a lithography defect at metal separation, and some exhibited unacceptably high finger resistance, owing to a combination of narrow n finger design and over-etch during contact separation etch. A total of nine 'good' cells were tested from this batch, each having a single-layer ARC (with the exception of the best cell reported here, which had DLARC applied subsequent to cell completion). Considerable variation in cell performance was observed, with median efficiency of 23.2% and standard deviation of 1.0% (in-house measurements). The cause of the variation between wafers and within a wafer is still under investigation; uniformity of front-surface passivation is believed to be the most likely candidate, with photoluminescence images taken immediately after SiN_x deposition showing significant variation across the wafer.

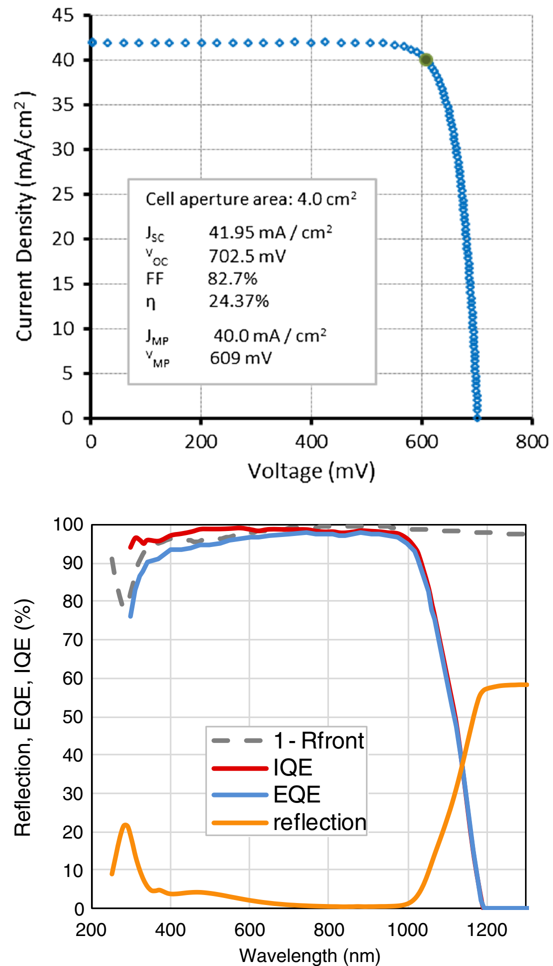

Figure 12. IV curve and characteristics of best cell, independently confirmed by Fraunhofer ISE CalLab (top) and corresponding reflectivity and quantum efficiency curves (bottom).

Figure 13 is a calibrated photoluminescence (PL) image of the wafer that contained the highest efficiency cell, taken immediately after nitride deposition, imaged at 1-sun photon flux and effective lifetime calibrated via quasi-steady-state photoconductance decay measurement. It is quite evident that effective lifetime varies significantly across the wafer and from cell to cell (approximate position indicated by the boxes). Indeed, such an image can be reliably used to predict relative cell performance, notwithstanding any shunts or contact problems that may be introduced during metallisation. Improved understanding of the reasons behind this variation could unlock potential efficiency gains or at least allow for better utilisation of each of the cell locations.

4.2. IBC cells incorporating laser processing

One batch of cells has been fabricated with contact formation via excimer laser ablation for part of the batch and contact openings completed via photolithography for the remaining wafers. Wafers were co-processed for all other

DOI: 10.1002/pip

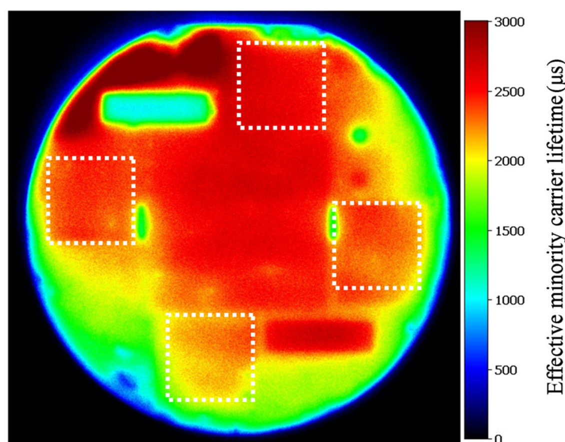

Figure 13. Calibrated photoluminescence image of wafer containing best cell, prior to contact opening and metallisation, at 1-sun photon flux. Square boxes overlaid on the image represent locations of each of the 2 × 2-cm^2 cells, with the 24.4% efficient cell located at the top of the image. Note that the central area corresponds to a single 4 × 4-cm^2 cell, not reported on in this work owing primarily to contact alignment problems.

processing steps, to facilitate direct comparison between ablation and photolithography, albeit with an approximately two times larger contact area for laser-processed cells. To facilitate comparison, the results presented in Table II for the best cell processed via each method are from in-house measurements because no independently verified measurement of the photolithography-based cell has been performed. The laser-processed cell has also been certified by Fraunhofer ISE CalLab with an efficiency value of 23.5 ± 0.7%, a V_{OC} of 696 mV, J_{SC} of 41.4 mA/cm^2 and fill factor of 81.7%. Importantly, the results show not only that efficiency is not reduced by the laser ablation route but also that voltage and fill factor are both also maintained. This suggests that the laser ablation process has not introduced significant recombination-active damage and has achieved good, low-resistance contacts.

Finally, a first batch of IBC cells featuring laser-doped local BSF and laser-doped local emitters only and utilising direct laser ablation for contact formation has been fabricated at ANU. In this case, the selection process for choice of appropriate laser parameters for performing doping was limited to a simple recombination analysis experiment based on non-metallised, unpassivated, broad-area doping only. The limitation of such a process is that recombination

Table II. Best cell results for photolithography and laser ablation contact formation from a co-processed batch of IBC cells.

Contact formation method	J_{SC} (mA cm^2)	V_{OC} (mV)	Fill factor	Efficiency*
Photolithography	40.94	698	82.7%	23.6%
Laser ablation	40.96	696	82.9%	23.6%

*Note: These are both in-house measurements; for ease of comparison, the certified result for the laser processed cell is 23.5%.

(both ideal and non-ideal) and shunting behaviour associated specifically with metallisation of laser-processed features, along with the possible edge effects associated with the perimeter of laser-doped regions, are overlooked. In cells fabricated as part of this work, this led to a dramatic increase in net recombination immediately after metallisation, evidenced by a considerable drop in photoluminescence count after metallisation (accounting for changes as a result of the altered optics). Cells also featured relatively poor contacting to phosphorus-doped regions, as indicated by the high contact resistances measured on dedicated contact resistivity test structures that were prepared on the same wafers as the cells. Nonetheless, we can report maximum efficiency of the first all-laser-doped and laser-contacted IBC cells of 19.1%, measured in-house. This cell, fabricated on 250-μm-thick 100-Ω cm p-type material, featured a V_{OC} of 671 mV, J_{SC} of 41.7 mA/cm^2 but a fill factor of only 68%. Future work in this area will utilise methods recently published on detailed characterisation of local laser-doped features [24], in which an efficiency potential of 24% has already been identified for all laser-doped cells.

5. DETAILED LOSS ANALYSIS FOR A 24.4% IBC CELL

In conducting a detailed loss analysis of our IBC cells, we focus our attention on the 24.4% efficient cell and consider each of the loss mechanisms that limit its performance. Such an analysis gives rise to obvious questions on how to increase efficiency further and provides guidance on which features of the cell to target first. This analysis relies upon accurate characterisation of the cell and process metrics to first quantify optical losses and thus provide a set of accurate photogeneration profiles for use in subsequent 3D device simulations via Quokka, which, in turn, is used to reveal specific recombination and resistive losses. Table III lists the cell parameters used in these simulations. With the exception of the bulk SRH lifetime parameter, which was unobtainable directly from the fully processed Cz wafer containing the 24.4% cell, all other parameters are either measured directly from the cell or wafer itself or are extracted from measurements on dedicated diffusion and passivation film monitor wafers that were co-processed through each of the relevant process steps. All modelling is conducted using a temperature of 25°C and an effective intrinsic carrier density $n_{i,eff}$ of 8.70×10^9/cm, as explained in Section 2.3. SRH bulk recombination with a fundamental electron and hole lifetime of $\tau_{n0} = \tau_{p0} = 5$ ms are used in simulations, as these provide a good fit between simulated and dark JV measurements of the cell (Figure 14) in particular around maximum power point, where SRH recombination has more influence compared with high-injection V_{OC} conditions. Finally, because the cells fabricated in this work are only 2 × 2 cm^2, edge losses, which are characterised by the diffusion of carriers out of the active cell area where they recombine in the bulk or at surfaces in the surrounding cell

Table III. Measured key properties of the 2×2-cm^2 24.4% efficient cell, used in 3D device modelling for detailed loss analysis.

Property	Measured value
Cell thickness	230 μm
Wafer resistivity	1.5 Ω cm
Bulk SRH lifetime	5000 μs
Rear pitch	500 μm
Emitter width	330 μm
BSF diameter/pitch	27 μm/70 μm
n contact diameter/pitch	7 μm/70 μm
p contact diameter/pitch	7 μm/70 μm
Emitter sheet R/J_0	166 Ω/□/36 fA/cm^2
BSF sheet R/J_0	19 Ω/□/190 fA/cm^2
Undiffused rear J_0	21 fA/cm^2
Front surface J_0	5 fA/cm^2
n contact J_0/ρ_c	280 fA/cm^2/~1×10^{-5} Ω cm^2
p contact J_0/ρ_c	810 fA/cm^2/~1.5×10^{-5} Ω cm^2
n finger/p finger width	134 μm/282 μm
Finger sheet resistance	6.3 mΩ/□

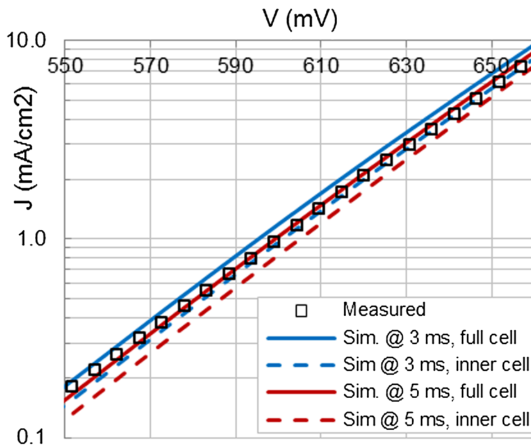

Figure 14. Measured and simulated (both *inner unit cell* and *full cell*) dark J–V curves of the 24.4% cell in the vicinity of maximum power point (610 mV), using simulated SRH bulk lifetimes of 3 and 5 ms and with all other simulation parameters from measurements of the physical, optical and electronic properties of the cell or corresponding test structures.

perimeter region, can be quite significant. We again use Quokka to model the loss of carriers to recombination outside of the active cell and hence determine cell edge losses.

The procedure employed for the comprehensive evaluation of optical losses, along with its application to this 24.4% IBC cell, is detailed by McIntosh *et al.* in [29]. Briefly, this involves combining reflectivity, spectrophotometry, ellipsometry and quantum efficiency measurements on the fabricated cell and a range of co-processed test structures with ray tracing and optical thin-film transfer matrix calculations to accurately quantify photogeneration current and 'lost' current owing to front-surface reflection, ARC absorption, non-ideal light trapping and free-carrier absorption as a function of incident light wavelength. For this cell, a photogeneration current density of 42.76 mA/cm^2 is calculated, with corresponding lost photon current densities of 0.58, <0.06, 0.8 and 0.05 mA/cm^2 for reflection, ARC absorption, non-ideal light trapping and free-carrier absorption respectively. We use ray tracing to create photogeneration profiles corresponding to each of these optical loss mechanisms being separately 'turned off', before carrying these forward into subsequent device simulations in order to accurately determine the efficiency losses by attributing the increased power output of the cell to the specific optical loss that has been 'turned off'.

Device modelling is conducted using Quokka 3D modelling specifically developed to simulate IBC cells and also incorporating detailed 'free energy loss analysis' (FELA) [53] to isolate and quantify each of the major loss mechanisms within the device [54]. The programme is also able to evaluate IBC cell edge losses using a parallel combination of *inner unit cells* and special *perimeter unit cells* that consists of non-active regions adjacent to the active cell area, so as to properly account for diffusion of carrier into and recombination of carriers within the perimeter region surrounding the cell. This approach has been validated via comparison with measurements under controlled experimental conditions [54]. For the '24.4% cell' modelled as part of this work, we arrive via this method at a modelled V_{OC}, J_{SC}, fill-factor and efficiency of 701 mV, 42.1 mA/cm^2, 83.1% and 24.5% which is well within measurement error in all respects to the measured characteristics. Loss in cell efficiency owing to recombination in the edge region outside the active cell area is easily calculated by taking the difference in efficiency of the *inner unit cell* and the complete *combined cell*. The *inner unit cell* is subsequently simulated again at the V_{mpp} of the combined cell to determine via FELA the power losses owing to each different recombination or resistive loss mechanisms.

A detailed breakdown of cell efficiency losses is provided in Figure 15. It can be seen that summing all losses and adding to cell efficiency yield a value of 27.9%. Such a value naturally approaches the limiting efficiency for silicon solar cells based on this resistivity and thickness, which has been calculated recently by Richter *et al.* as being close to 28.7% for 230-μm-thick 1.5-Ω cm n-type cells. [39]. We also observe, by simulating the cell with ideal optics and elimination of all but Auger and radiative recombination losses, a limiting efficiency value of 28.45%, where the difference is attributed to resistive losses not considered in the Richter limit. The sum of the losses does not meanwhile equate to this limiting value because the losses are specific to a particular operating point of the cell, which clearly would shift (to a higher carrier density regime and ultimately higher voltage) if each of the losses was to be removed. In particular, the entropy losses are not included in the loss breakdown, which will necessarily be larger at lower voltages and consequently lower Fermi-level splitting [55,56]. Optical losses represent 0.86% absolute efficiency loss,

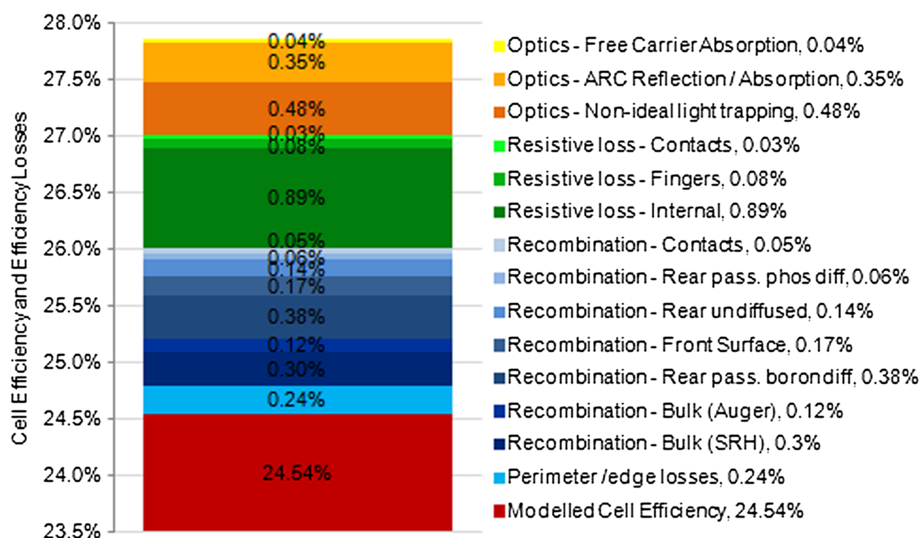

Figure 15. Modelled cell efficiency and detailed breakdown of all losses for the 24.4% efficient IBC cell. Modelling is conducted via Quokka 3D device simulation and optical ray tracing and utilises the free energy loss analysis method, with modelling inputs based on the measured physical, electronic and optical properties of the cell itself, accompanying test structures or co-processed monitor wafers (provided in Table III).

with resistive loss within the active cell area totalling about 0.99% and being mostly dominated by carrier transport in the bulk (resistive loss in the diffusion being negligible). Recombination within the active cell area represents a further 1.22% absolute efficiency loss, dominated by recombination in the bulk, in the emitter and at the front surface, with an absolute efficiency loss of 0.24% owing to edge losses outside of the active cell area (recombination and resistive). The results suggest that the most significant gains can be realised by improving material quality, optics and surface passivation; this would also reduce the internal resistive losses as the injection level and thus carrier conductivities would be increased.

6. CONCLUSIONS

Interdigitated back contact cells offer a clear route to very high efficiency values. Optimisation of detailed cell design, and hence also cell fabrication processes, for maximum efficiency is dependent upon material availability and achievable process outcomes. For cells fabricated as part of this work, 166-Ω/□ boron emitters with coverage fraction of 66% and 19-Ω/□ locally diffused phosphorus BSFs were formed on 230-μm-thick 1.5-Ω cm n-type substrate, with 500-μm pitch and small contact fraction. Cells feature PECVD SiN_x and SiO_2/LPCVD Si_3N_4 for front and rear-surface passivation respectively, with an independently confirmed 4-cm^2 designated-area efficiency of 24.4% recorded. We have shown the potential for process simplification by laser processing, with ablation of dielectric layers for contact formation incorporated into IBC cell fabrication to yield an efficiency value of 23.5%. Furthermore, we demonstrated a preliminary efficiency value of 19% for IBC cells featuring laser-doped local BSF and laser-doped local emitter only and contact formation via laser ablation.

A detailed loss analysis of the best cell has been conducted, facilitated by accurate 3D simulation based on the measured optical, electronic and physical properties of the cell. This revealed that edge losses are significant (0.24% absolute efficiency loss), while recombination, resistive and optical losses in total amount to 1.23, 0.87 and 1.00% respectively. Considerable efficiency gains can be made by using better quality material, improving light trapping via surface treatments, by improvement of rear passivation quality, and by better understanding of and mitigation of edge losses. Fabrication of 25+% efficient cells at ANU is an achievable near-term goal.

ACKNOWLEDGEMENTS

This work was performed at ANU under a research contract for Trina Solar and through a joint research project between Trina Solar and the Solar Energy Research Institute of Singapore (SERIS). SERIS is sponsored by the National University of Singapore and Singapore's National Research Foundation through the Singapore Economic Development Board. This work is supported by the National High-Tech R&D Program (863 program) of the Ministry of Science and Technology of China under project number 2012AA050303.

This programme has been supported by the Australian Government through the Australian Renewable Energy Agency. Responsibility for the views, information or advice expressed herein is not accepted by the Australian Government.

The authors would like to thank Christian Reichel, Jochen Hohl-Ebinger and Elisabeth Schaeffer at Fraunhofer ISE for assistance with calibrated IV and IQE measurements.

REFERENCES

1. Swanson RM, Beckwith SK, Crane RA, Eades WD, Young HK, Sinton RA, Swirhun SE. Point-contact silicon solar cells. *IEEE Transactions on Electron Devices* 1984; **31**: 661–664.
2. Verlinden PJ, Sinton RA, Wickham K, Crane RA, Swanson RM. Backside-contact silicon solar cells with improved efficiency for the `96 world solar challenge. *14th EPVSC*, Barcelona, 1997; 96–99.
3. Cousins P, Smith D, Luan H, Manning J, Dennis T, Waldhauer A, Wislon K, Harley G, Mulligan W. Generation 3: Improved performance at lower cost. *25th EUPVSEC*, Valencia, 2010; 275–278.
4. Fong KC, Kho T, McIntosh K, Blakers A, Franklin E, Zin N, Fell A. Optimisation of N+ diffusion and contact size of IBC solar cells. *28th EU PVSEC*, Paris, 2013; 851–854.
5. Coveme spa. EBFOIL Range datasheets. http://www.coveme.com/ebfoil-range [accessed 30 June 2014]
6. Bennett I, Erenstein W, Rosca V. Reducing the Cost of Back-Contact Module Technology. *Energy Procedia* 2013; **38**: 329–333.
7. Taguchi M, Yano A, Tohoda S, Matsuyama K, Nakamura Y, Nishiwaki T, Fujita K, Maruyama E. 24.7% Record Efficiency HIT Solar Cell on Thin Silicon Wafer. *IEEE Journal of Photovoltaics* 2014; **4**(1): 96–99.
8. Tsunomaru Y, Yoshimine Y, Taguchi M, Baba T, Kinoshita T, Kanno H, Sakata H, Maruyama E, Tanaka M. Twenty-two percent efficiency HIT Solar Cell. *Solar Energy Materials and Solar Cells* 2009; **93**(6): 670–673.
9. Green M. The path to 25% silicon solar cell efficiency: History of silicon cell evolution. *Progress in Photovoltaics* 2009; **17**(3): 183–189.
10. Masuko K, Shigematsu M, Hashiguchi T, Fujishima D, Kai M, Yoshimura N, Yamaguchi T, Ichihashi Y, Mishima T, Matsubara N, Yamanishi T, Takahama T, Taguchi M, Maruyama E, Okamoto S. Achievement of more than 25% conversion efficiency with crystalline silicon heterojunction solar cell. *IEE Journal of Photovoltaics*, Denver, 2014.
11. Nakamura J, Katayama H, Koide N, Nakamura K. Development of Hetero-Junction Back Contact Si Solar Cells. *40th IEEE PVSC*, Denver, 2014.
12. Smith D, Cousins P, Westerberg S, Jesus-Tabajonda R, Aniero G, Shen Y. Towards the Practical Limits of Silicon Solar Cells, *IEEE Journal of Photovoltaics*, 2014.
13. Reichel C, Granek F, Hermle M, Glunz S. Back-contacted back-junction n-type silicon solar cells featuring an insulating thin film for decoupling charge carrier collection and metallization geometry. *Progress in Photovoltaics* 2013; **21**: 1063–1076.
14. Peibst R, Harder N-P, Merkle A, Neubert T, Kirstein S, Schmidt J, Dross F, Basore PA, Brendel R. High-efficiency RISE IBC solar cells: influence of rear side passivation on pn junction meander recombination. *28th EU PVSEC*, Paris, 2013.
15. O'Sullivan B, Debucquoy M, Singh S, Uruena de Castro A, Récaman-Payo M, Posthuma N, Poortmans J. Process Simplification for High Efficiency, Small area IBC silicon solar cells. *28th EU PVSEC*, Paris, 2013.
16. Aleman M, Das J, Janssens T, Pawlak B, Posthuma N, Robbelein J, Singh S, Baert K, Poortmans J, Fernandez J, Yoshikawa K, Verlinden PJ. Development and Integration of a High Efficiency Baseline Leading to 23% IBC Cells. *Energy Procedia* 2012; **27**: 638–645.
17. Dahlinger M, Bazer-Bachi B, Roder T, Kohler J, Zapf-Gottwick R, Werner J. 22.0% Efficient Laser Doped Back Contact Solar Cells. *Silicon PV Conference*, Hamelin, Germany, 2013.
18. Press Release Trina Solar, 28 February 2014. http://ir.trinasolar.com/phoenix.zhtml?c=206405&p=irol-newsArticle&ID=1904732&highlight= [accessed 1 September 2014]
19. Zhang X, Yang Y, Liu W, Zhang K, Chen Y, Li Z, Xu G, Jiao H, Zhang S, Feng Z, Verlinden PJ. Development of High Efficiency Interdigitated Back Contact Silicon Solar Cells and Modules with Industrial Processing Technologies. *6th World Conference on Photovoltaic Energy Conversion*, Kyoto, 2014.
20. Press release BOSCH Solar Energy, 14 August 2013. http://www.solarserver.com/solar-magazine/solar-news/archive-2013/2013/kw33/bosch-isfh-produce-221-efficient-c-si-solar-pv-cell.html [accessed 1 September 2014]
21. Mo CB, Park SJ, Kim YJ, Lee DY, Park SC, Kim DS, Kim SB, Graff J, Sheoran M, Sullivan P. *Presentation at 27th. European Photovoltaic Solar Energy Conference*, Munich, 2012.
22. Lammert MD, Schwartz RJ. The Interdigitated Back Contact Solar Cell: Silicon Solar Cell for Use in Concentrated Sunlight. *IEEE Transactions on Electron Devices* 1977; **24**(4): 337–342.
23. Reichel C, Granek F, Hermle M, Glunz S. Investigation of electrical shading effects in back-contacted back-junction silicon solar cells using the two-dimensional charge collection probability and the reciprocity theorem. *Journal of Applied Physics* 2011; **109**: 024507.

24. Fell A, Surve A, Franklin E, Weber K. Characterisation of Laser-Doped Localised p-n Junctions for High Efficiency Silicon Solar Cells. *IEEE Transactions on Electron Devices* 2014; **61**(6): 1943–1949.
25. Haase F, Eidelloth S, Horbelt R, Bothe K, Garralaga Rojas E, Brendel R. Loss analysis of back-contact back-junction thin-film monocrystalline silicon solar cells. *Journal of Applied Physics* 2011; **110**: 124510.
26. Kulushich G, Zapf-Gottwick R, Werner J. Numerical Simulation of Fully Laser Processed Back-Contact Back-Junction Solar Cells. *Proceedings of the 26th European Photovoltaic Solar Energy Conference*, Hamburg, Germany, 2011; 275–280.
27. McIntosh KR, Baker-Finch SC. OPAL 2: Rapid optical simulation of silicon solar cells. *Proc. 38th IEEE PVSC*, Austin, 2012; 265–271.
28. PV Lighthouse. http://www.pvlighthouse.com.au/calculators/ [accessed 23 June 2014]
29. McIntosh K, Kho T, Fong K, Baker-Finch S, Wan Y, Zin N, Franklin E, Wang D, Abbott M, Grant N, Wang E, Stocks M, Blakers A. Quantifying the optical losses in back-contact solar cells. *40th IEEE PVSC*, Denver, 2014.
30. Zin N, Fong K, Franklin E, Kho T, Grant N, Wang D, Wang E. Etchback simplifies Interdigitated Back Contact Solar Cells. *40th IEEE PV Specialists Conference*, Denver, 2014.
31. McIntosh K, Cudzinovic M, Smith D, Mulligan W. The choice of silicon wafer for the production of low-cost rear-contact solar cells. *Proceedings of 3rd World Conference on Photovoltaic Energy Conversion*, 2003; 971–974.
32. Smith D, Cousins P, Masad A, Westerberg S, Defensor M, Ilaw R, Dennis T, Daquin R, Bergstrom N, Leygo A, Zhu X, Meyers B, Bounre B, Shields M, Rose D. SunPower's Maxeon Gen III solar cell: High Efficiency and Energy Yield. *39th IEEE PVSC*, Tampa Bay, 2013.
33. Swanson RM. Point-Contact Solar Cells: Modeling and Experiment. *Solar Cells* 1986; **17**(1): 85–118.
34. Granek F, Hermle F, Huljic D, Schultz-Wittman O, Glunz S. Enhanced Lateral Current Transport Via the Front n+ Diffused Layer of n-type High-efficiency Back-junction Back-contact Silicon Solar Cells. *Progress in Photovoltaics: Research and Applications* 2008; **17**(1): 47–56.
35. Wan Y, McIntosh K, Thomson A, Cuevas A. Low surface recombination velocity by low-absorption silicon nitride on c-Si. *IEEE JPV* 2013; **3**: 554–559.
36. Thomson A, Grant N, Fong K, Kho T. Improved Diffused-Region Recombination-Current Pre-Factor Analysis. *4th International Conference on Silicon PV*, 's-Hertogenbosch, 2014.
37. Kane D, Swanson R. Measurement of the Emitter Saturation Current by a Contactless Photoconductivity Decay Method. *Proceedings of the 18th IEEE Photovoltaic Specialists Conference*, 1985; 578–583.
38. Schenk A. Finite-Temperature Full Random-Phase Approximation Model of Band Gap Narrowing for Silicon Device Simulation. *Journal of Applied Physics* 1998; **84**: 3684–3695.
39. Richter A, Hermle M, Glunz S. Reassessment of the Limiting Efficiency for Crystalline Silicon Solar Cells. *IEEE Journal of Photovoltaics* 2013; **3**(4): 1184–1191.
40. Cuevas A, Yan D. Misconceptions and misnomers in Solar Cells. *IEEE Journal of Photovoltaics* 2013; **3**(2): 916–923.
41. Williams K, Gupta K, Wasilik M. Etch Rates for Micromachining Processing – Part II. *Journal of Microelectromechanical Systems* 2003; **12**(6): 761–778.
42. Reeves GK, Harrison HB. Obtaining the specific contact resistance from transmission line model measurements. *Electron Device Letters, IEEE* 1982; **3**(5): 111–113.
43. Fell A, A Free and Fast Three-Dimensional/Two-Dimensional Solar Cell Simulator Featuring Conductive Boundary and Quasi-Neutrality Approximations. *IEEE Transactions on Electron Devices* 2013; **60**(2): 733–738.
44. Brendel R. Modeling solar cells with the dopant-diffused layers treated as conductive boundaries. *Progress in Photovoltaics* 2012; **20**(1): 31–43.
45. Grant N, McIntosh K, Tan J. Evaluation of the Bulk Lifetime of Silicon Wafers by Immersion in Hydrofluoric Acid and Illumination. *ECS Journal of Solid State Science and Technology* 2012; **1**(2): 55–61.
46. Phang S, Macdonald D. Direct comparison of boron, phosphorus, and aluminum gettering of iron in crystalline silicon. *Journal of Applied Physics* 2011; **109**: 073521
47. Halm A, Mihailetchi V, Galbiati G, Koduvelikulathu L, Roescu R, Comparotto C, Kopecek R, Peter K, Libal J. The Zebra Cell Concept – large Area n-type Interdigitated Back Contact Solar Cells and One-Cell Modules Fabricated Using Standard Industrial Processing Equipment. *Proceedings of the 27th EUPVSC*, Frankfurt, 2012; 567–570.
48. Engelhart P, Harder N, Grischke R, Merkle A, Meyer R, Brendel R. Laser Structuring for Back Junction Silicon Solar Cells. *Progress in Photovoltaics* 2007; **15**: 237–243.
49. Engelhart P, Hermann S, Neubert T, Plagwitz H, Grischke R, Meyer R, Klug U, Schoonderbeek A, Stute U, Brendel R. Laser ablation of SiO2 for locally contacted Si solar cells with ultra-short pulses. *Progress in Photovoltaics* 2007; **15**: 521–527.
50. Knorz A, Peters M, Grohe A, Harmel C, Preu R. Selective laser Ablation of SiN_x Layers on Textured Surfaces for Low Temperature Front Side Metallizations. *Progress in Photovoltaics* 2008; **17**: 127–136.

51. Walter D, Fell A, Franklin E, Wang D, Fong K, Kho T, Weber K, Blakers A. Damage-free ultraviolet nanosecond laser ablation for high efficiency back contact solar cell fabrication. *Solar Energy Materials and Solar Cells* 2014 [Submitted].
52. Filmtronics Inc. www.filmtronics.com [accessed June 2014]
53. Brendel R, Dreissigacker S, Harder N-P, Altermatt PP. Theory of analyzing free energy losses in solar cells. *Applied Physics Letters* 2008; **93**: 173503.
54. Fell A, Fong K, McIntosh K, Franklin E, Blakers A. 3-D Simulation of Interdigitated-Back-Contact Silicon Solar Cells With Quokka Including Perimeter Losses. *IEEE Journal of Photovoltaics* 2014; **4**(4): 1040–1045.
55. Wurfel P. *Physics of Solar Cells: From Basic Principles to Advanced Concepts*. Wiley: Weinheim, 2009.
56. Greulich J, Hoffler H, Wurfel U, Rein S. Numerical power balance and free energy loss analysis for solar cells including optical, thermodynamic, and electrical aspects. *Journal of Applied Physics* 2013; **114**: 204504.